OCEANOGRAPHY

The competition between anthropogenic aerosol and greenhouse gas climate forcing is revealed by North Pacific water-mass changes

Jia-Rui Shi[1]*, Susan E. Wijffels[1], Young-Oh Kwon[1], Lynne D. Talley[2], Sarah T. Gille[2]

Modeled water-mass changes in the North Pacific thermocline, both in the subsurface and at the surface, reveal the impact of the competition between anthropogenic aerosols (AAs) and greenhouse gases (GHGs) over the past 6 decades. The AA effect overwhelms the GHG effect during 1950–1985 in driving salinity changes on density surfaces, while after 1985 the GHG effect dominates. These subsurface water-mass changes are traced back to changes at the surface, of which ~70% stems from the migration of density surface outcrops, equatorward due to regional cooling by AAs and subsequent poleward due to warming by GHGs. Ocean subduction connects these surface outcrop changes to the main thermocline. Both observations and models reveal this transition in climate forcing around 1985 and highlight the important role of AA climate forcing on our oceans' water masses.

INTRODUCTION

The global hydrological cycle is enhanced due to anthropogenic warming of the global surface and lower atmosphere based on theory and models (*1*–*4*). This results in a pattern amplification of evaporation minus precipitation as the warmer air can hold and transport more water vapor (*4*–*6*). From an oceanic perspective, the "fresh gets fresher, salty gets saltier" pattern of salinity expresses a fingerprint of this intensifying water cycle (*7*–*13*). Historical ocean observations provide valuable information used to detect and understand this anthropogenically induced change to the hydrological cycle (*9*, *13*), which has been more difficult to detect in the sparse and noisy observational record of rainfall and evaporation. In terms of ocean temperature change, the near-surface ocean has warmed, especially since about 1950. Surface warming (and freshening) can lead to a poleward shift of the location of an isopycnal (i.e., a surface of constant potential density) outcrop. Compared with the effect of salinity amplification, the broad-scale warming in the subtropics dominates outcrop migration (*14*). It has been found that this outcrop migration is an important factor in explaining the water-mass changes in density space because the strongest change appears in the high-gradient regions of the climatological mean surface salinity (*15*). Although the global ocean warming was monotonic, the historic migration of isopycnal outcrops has not been unidirectional in some regions, e.g., the North Pacific, as discussed in this study, and the outcrop migration effect on water-mass changes remains to be quantified.

Greenhouse gases (GHGs) and anthropogenic aerosols (AAs) are two major anthropogenic forcing agents that have driven historical climate change (*16*–*22*). For instance, more than 90% of the excess heat taken up by the Earth system since 1970 is stored in the ocean, which is an excellent indicator of the aggregate warming effect dominated by GHG forcing (*23*, *24*). On the other hand, the substantial emissions of AA after World War II are cooling the Earth (*25*, *26*) and can compensate for part of the GHG-induced warming. AAs can also give rise to characteristic regional climate responses, such as a shift of the intertropical convergence zone linked with an AA-induced interhemispheric energy imbalance, Sahel drought and recovery, and changes in trade winds and the Walker circulation (*27*–*31*). Recently, the Pacific Ocean has attracted much attention in terms of the substantial changes or oscillations induced by AA forcing (*32*–*37*). Therefore, the detectability of an aerosol climate effect could be higher in the Pacific basin, especially in the North Pacific, which is close to the present largest source of emissions in the Northern Hemisphere.

Because AA has been an essential forcing agent in historical climate change, it should have left its long-lasting "fingerprints" in the ocean, whose adjustment time to surface forcing is decades to centuries. However, unlike GHG forcing, the AA fingerprints recorded in the interior ocean have remained unclear to date. In this study, we investigate Pacific thermocline water-mass change (by which we mean the modification of the temperature-salinity relationship), which provides an alternative viewpoint of the temperature and salinity changes commonly diagnosed on pressure surfaces. It also provides a clear linkage between surface and subsurface responses through natural wind-driven subduction (*15*, *38*) and may reveal the respective contributions from these two major anthropogenic forcings.

RESULTS

Observed water-mass changes in the Pacific

Salinity changes diagnosed on an isopycnal can be used to distinguish water-mass changes from the changes driven by the vertical movement of isopycnals (referred to as heave) that a planetary wave or eddy may cause (*14*, *39*). In the zonal average, the North Pacific thermocline ($\sigma_1 < 31$ kg m^{-3}) shows opposing trends of observed salinity change along isopycnals in the period 1950–1985 compared to 1985–2014 (Fig. 1). This is found consistently in two different historical data products: the EN4 product from the Met Office Hadley Centre and the IAP product from the Institute of Atmospheric Physics (*40*, *41*). This nonmonotonic water-mass change

[1]Woods Hole Oceanographic Institution, Woods Hole, MA, USA. [2]Scripps Institution of Oceanography, University of California San Diego, La Jolla, CA, USA.
*Corresponding author. Email: jshi@whoi.edu

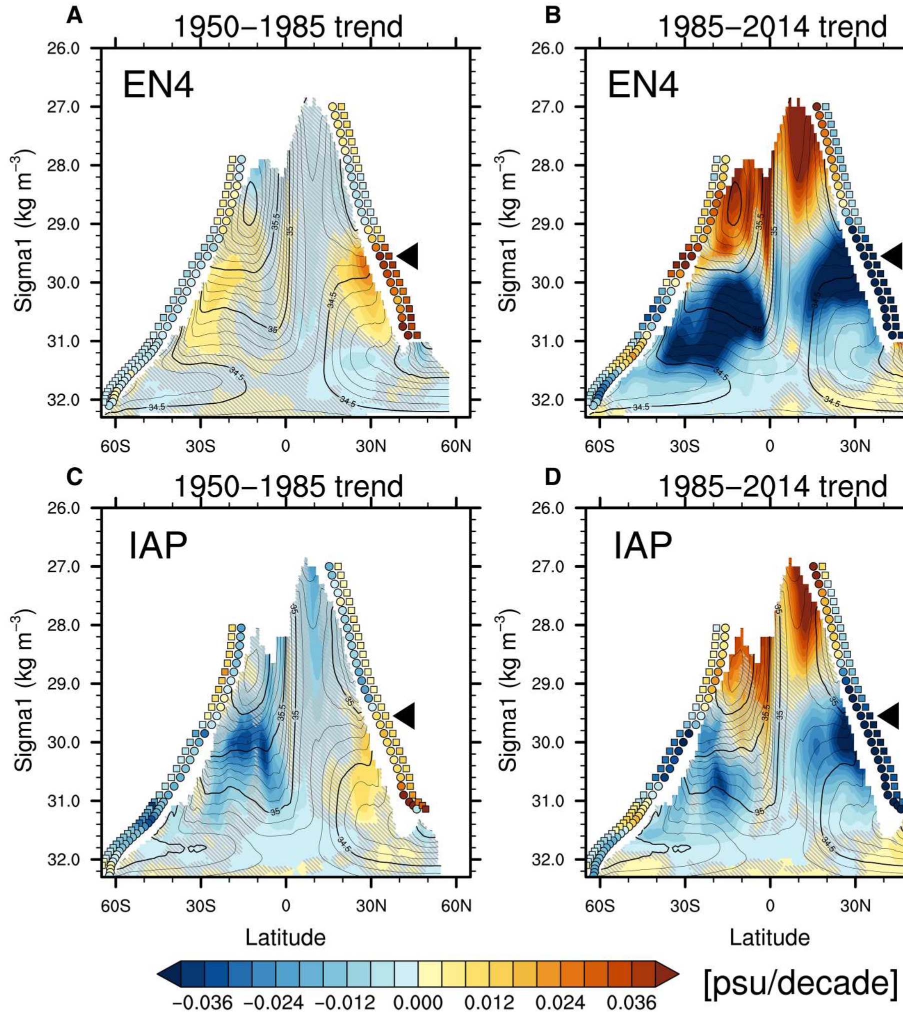

Fig. 1. Zonally averaged observed salinity trends in density space in the Pacific basin. Salinity trends [colors, practical salinity unit (psu)/decade] from the EN4 product for (**A**) 1950–1985 and (**B**) 1985–2014. (**C** and **D**) Observed salinity trends from the IAP product. Climatological annual mean salinity is shown as black contours, with thicker contours in every 0.5 psu. Circles are winter surface salinity anomalies at the salinity front (dS_{outcrop}), and squares are the salinity anomalies due to the outcrop meridional shift (dS_{shift}; psu/decade). Black triangles indicate the density level where the mean surface salinity meridional gradient is the maximum (with negative values), i.e., the salinity front, in the North Pacific. Regions where the linear trend is not significant at the 95% confidence level are hatched in gray.

contrasts with many indices dominated by a largely monotonic GHG forcing (*21*). In addition, the freshening at around σ_1 = 30.0 kg m^{-3} during 1985–2014 is stronger than the salinity increase during 1950–1985.

As found previously (*15*), subsurface ocean changes are often tightly linked to salinity changes upstream at the surface outcrops of subducting isopycnals (circles in Fig. 1, hereafter dS_{outcrop}), reflecting the role of ocean subduction in the penetration of surface signals into the thermocline. These outcrop salinity changes are largely explained by the meridional shift of isopycnals through the background mean surface salinity field (squares in Fig. 1, hereafter dS_{shift}), primarily due to changing surface temperature. For instance, when an outcrop migrates away from the surface subtropical salinity maximum, freshening results. Therefore, the observed increase and subsequent decrease of salinity on the isopycnal surfaces that outcrop poleward of the surface salinity maximum reflect the equatorward and then poleward shifts of the outcrop. This migration of outcrops is associated with a corresponding surface cooling and subsequent warming (fig. S1). It is associated with the phase change of the Pacific Decadal Oscillation, which includes both internal variability and externally forced components. A strong fingerprint of this process (*15*) is that the maximum subsurface trends occur along isopycnals that outcrop in the vicinity of the surface salinity front (strong meridional gradient)—around 30°N (indicated by the black triangles in Fig. 1 and fig. S2) in the Pacific. These results confirm that isopycnal migration is more consequential for thermocline salinity trends than surface salinity variation. Furthermore, the agreement between the diagnosed changes following the outcrop at the surface and those found in the subsurface along isopycnals strongly hints that the salinity anomalies in the ventilated thermocline originate at the surface and are spread to the interior via subduction.

In the map depicting salinity trends on the density surface of the aforementioned salinity front, the North Pacific exhibits a strong and widespread salinification during the former period and freshening during the latter period (Fig. 2). Once again, it is confirmed that outcrop migration is the dominant driver of salinity change at the outcrops. The strong signals are concentrated in the central North Pacific (170°E to 130°W) close to the region of the Central Mode Water (*42*), where the isopycnal outcrops undergo substantial migration (fig. S1). These signals at outcrops then penetrate westward and equatorward into the ocean interior, following the known geostrophic flow pathways (*43*, *44*). This penetration from subtropics to tropics is also evident in the Hovmöller diagram about the salinity anomalies along an isopycnal (fig. S3). These figures support the idea that mean subduction associated with the ventilated thermocline spreads the surface changes into the gyres.

There are some noteworthy differences between the two observational products. While the long-term trends in the North Pacific share a similar pattern, they have different magnitudes, which provide a coarse indication of the observational uncertainty. The trends in the Southern Hemisphere show different signs during 1950–1985, with EN4 featuring an increase in salinity, but IAP a broad freshening (Fig. 1, A and C). In addition, there is a disagreement between the surface and subsurface changes from EN4 in the Southern Hemisphere: The surface has experienced a weak freshening around 30°S and 30.0 kg m^{-3}, but significant positive trends occurred in the corresponding subsurface regions. We contend that these larger differences in the South Pacific stem from the severe sparseness of observations during the earlier period such that the results are highly sensitive to differences in interpolation and gap-filling methods. In contrast, the stronger agreement in the North Pacific reflects the larger amount of pre-1985 hydrographic data available in that basin.

Anthropogenic effects diagnosed from CMIP6 experiments

Historical all-forcing simulations from 10 models (table S1) of the sixth phase of the Coupled Model Intercomparison Project (CMIP6) appear to reproduce many of the above observed features in North Pacific water-mass change. During 1950–1985, most models produce a salinification in the subtropical North Pacific thermocline water masses (fig. S4). In contrast, many models show freshening during 1985–2014 (fig. S5) in the region characterized by high climatological mean salinity. We also find that the maximum water-mass change occurs at different mean densities in different models, but in all models, water-mass change commonly originates from the surface region of the salinity front for that model (black triangles in figs. S4 and S5). Moreover, along with the consistent responses at the outcrop, the aforementioned isopycnal migration mechanism appears to be operating in the models as well.

One notable difference between the models and observations is the lack of increasing salinity in the past 30 years in the shallow thermocline layers (σ_1 < 29 kg m^{-3}) that outcrop equatorward of the

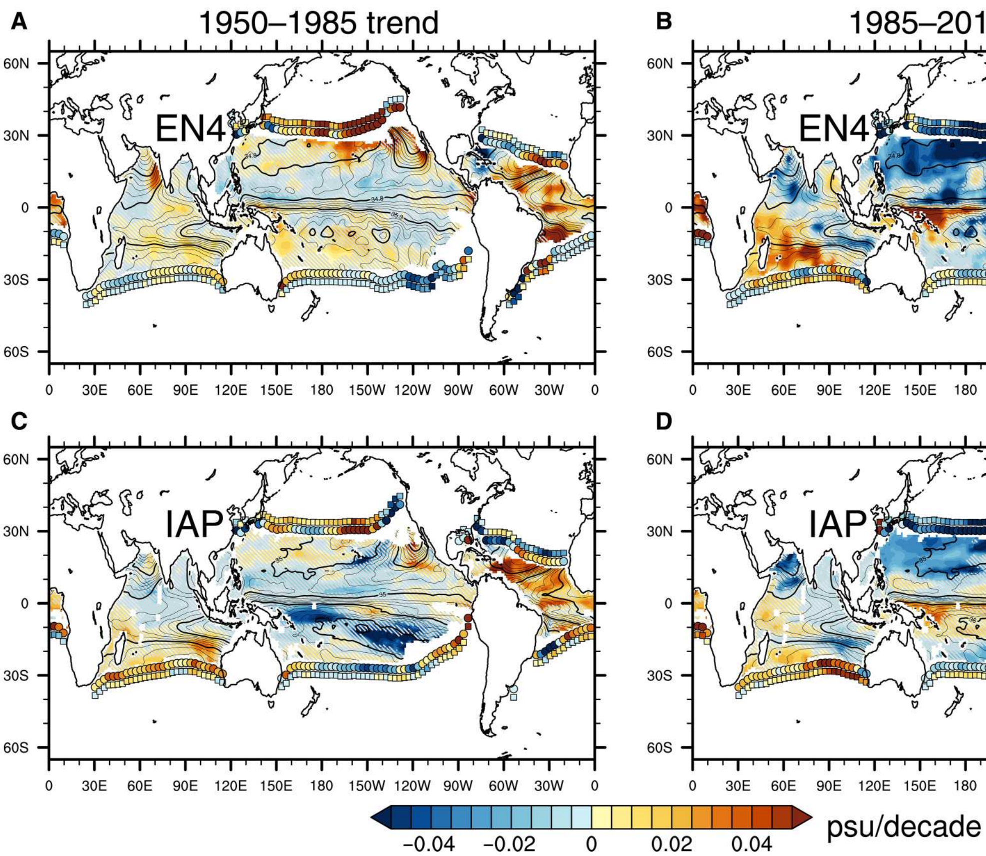

Fig. 2. Observed salinity trends at the density level of the North Pacific salinity front. Salinity trends (colors, psu/decade) from (**A** and **B**) EN4 and (**C** and **D**) IAP. Circles are winter dS_{outcrop}, and squares are winter dS_{shift} (psu/decade). Climatological annual mean salinity is shown as black contours, with thicker contours in every 0.5 psu. The density level is indicated by the black triangle in Fig. 1.

salinity maxima. While three models show weak salinification (compared to the observations), these layers largely freshen in the other models. One potential explanation is that near-surface tropical freshening could be diffused into the upper thermocline in the models more than occurs in nature. The strong tropical natural variability can be another important factor here.

To isolate the roles of AAs and GHGs in these simulated historical responses, we analyze the trends from single-forcing runs, i.e. AER and GHG runs, respectively (see Materials and Methods). AER runs show significant positive salinity trends in the North Pacific thermocline in each model over 1950–1985 (Fig. 3), which are associated with the equatorward shift of isopycnals due to local surface cooling. Within the same period, GHG runs show the opposite response due to the induced surface warming (fig. S6), although the magnitude of the change is smaller than that from AER runs in this period. Hence, the aerosol effect dominates the historical response during this early period (fig. S4). In contrast, after around 1985, the freshening induced by GHGs alone (Fig. 4) overwhelms the salinification from AAs alone (fig. S7), resulting in an overall freshening signal in HIST all-forcing runs (fig. S5). We thus see a competition between AAs and GHGs in driving changes in North Pacific thermocline water masses, with AA cooling dominating before 1985 and GHG warming afterward. In addition to the zonal mean approach used to reduce background noise, the salinity trend maps from CMIP6 models (fig. S8) align with the patterns observed (Fig. 2), highlighting the clear and dominant effects of aerosol and GHG forcings during different periods.

The wide variation in mean water-mass spatial structure between models is an obstacle to directly comparing a multimodel mean (MMM) section of the simulated results with observations. Given that, we focus on the salinity anomalies at the outcrop ($S_{outcrop}$) found at the surface salinity front (shown as black triangle in figures) in each model to investigate the detailed time evolution of these changes. The MMM of $S_{outcrop}$ in the historical runs

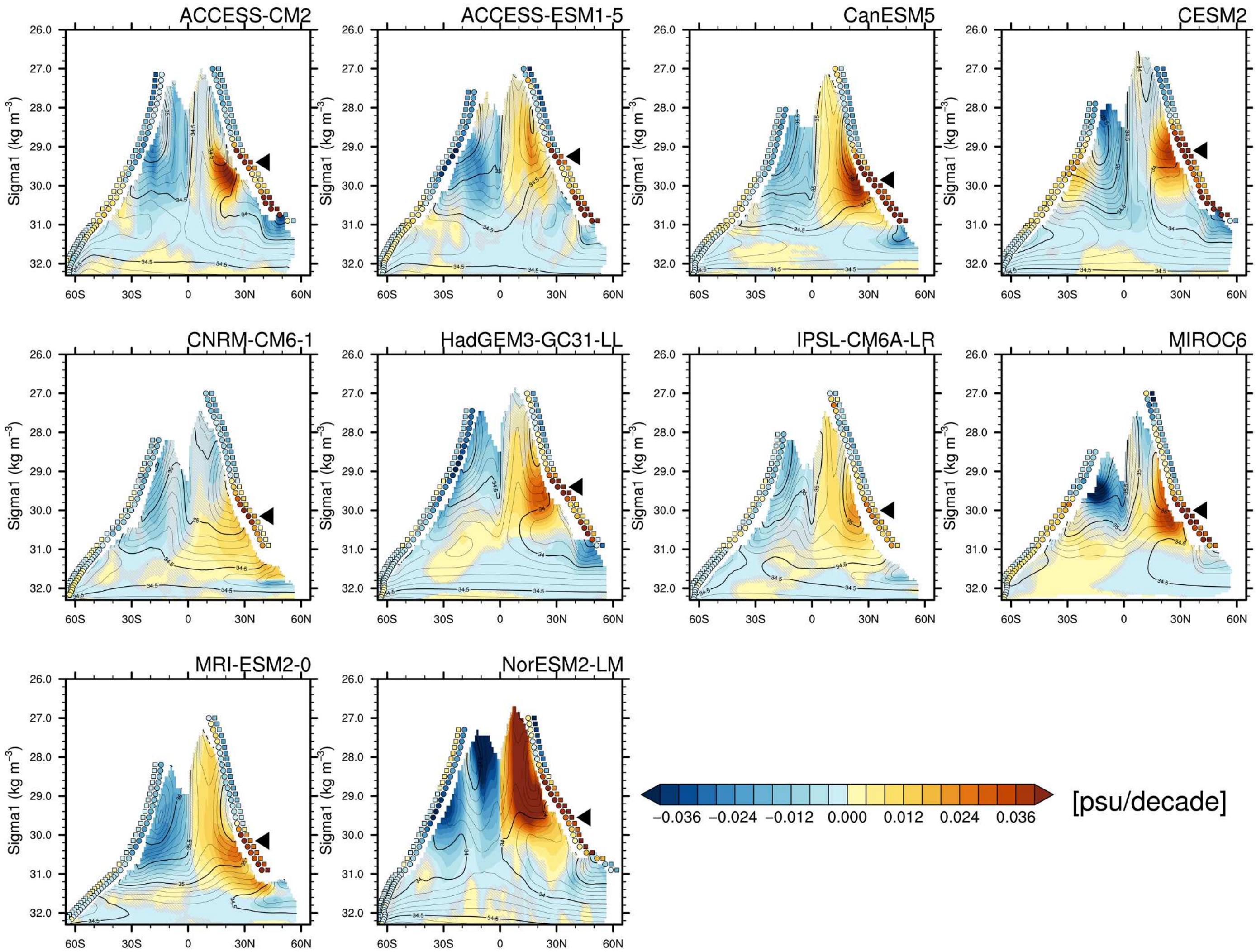

Fig. 3. Zonally averaged salinity trends (1950–1985) in density space in the Pacific basin from AER single-forcing runs for each CMIP6 model. Climatological annual mean salinity is shown as black contours, with thicker contours in every 0.5 psu. Circles are winter surface salinity anomalies at the salinity front ($dS_{outcrop}$), and squares are the salinity anomalies due to the outcrop meridional shift (dS_{shift}; psu/decade). Black triangles indicate the salinity front in the North Pacific. Regions where the linear trend is not significant at the 95% confidence level are hatched in gray.

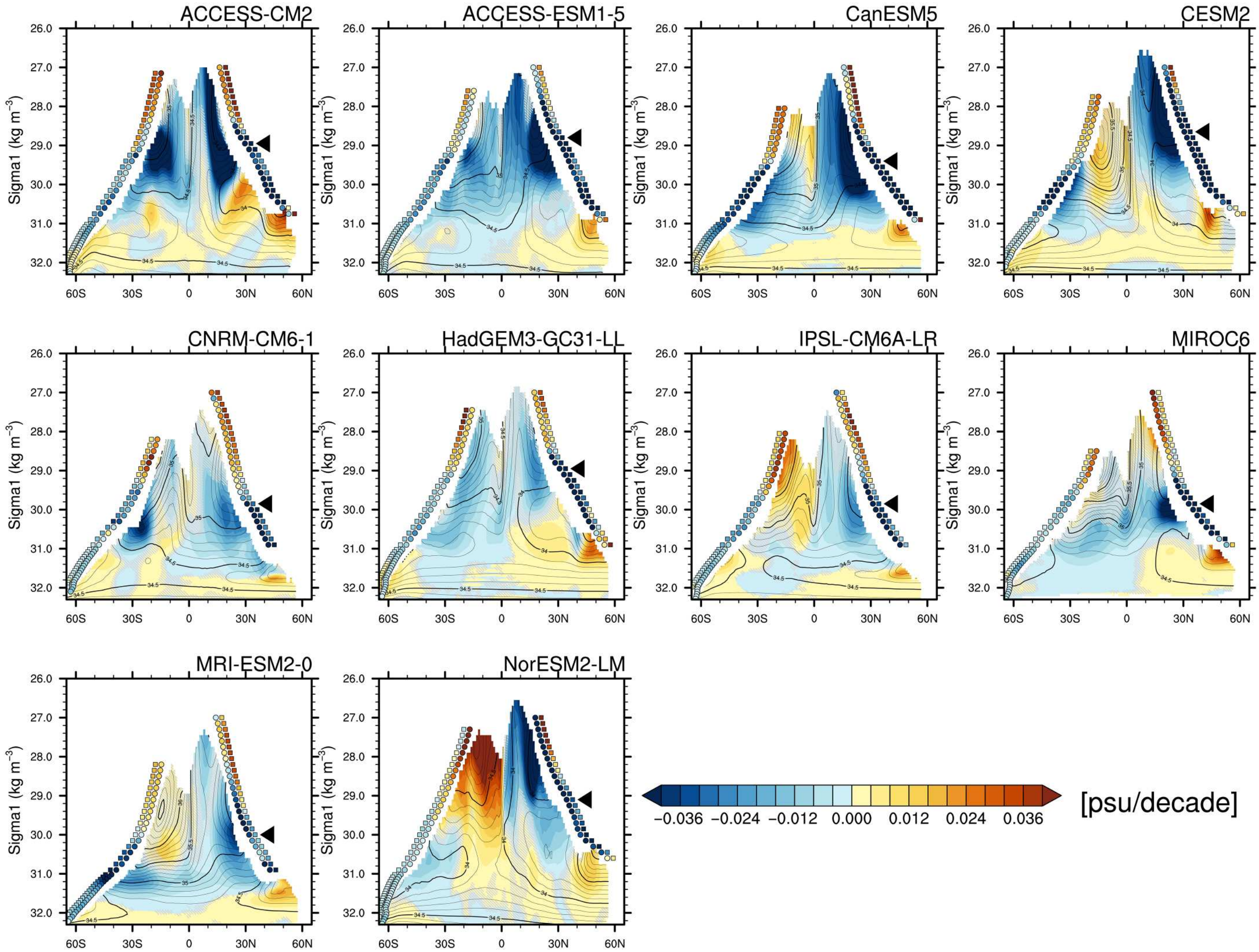

Fig. 4. Zonally averaged salinity trends (1985–2014) in density space in the Pacific basin from GHG single-forcing runs for each CMIP6 model. Climatological annual mean salinity is shown as black contours, with thicker contours in every 0.5 psu. Circles are winter surface salinity anomalies at the salinity front (dS_{outcrop}), and squares are the salinity anomalies due to the outcrop meridional shift (dS_{shift}; psu/decade). Black triangles indicate the salinity front in the North Pacific. Regions where the linear trend is not significant at the 95% confidence level are hatched in gray.

shows a clear nonmonotonic response of salinity in density space (black curve in Fig. 5A). This nonmonotonic behavior is evident in the migration of the outcropping latitudes (Fig. 5C) and thus the salinity change driven by such meridional migration (S_{shift}) (Fig. 5B). Notably, the two observation-based datasets are generally consistent with the CMIP6 MMM. We note that there are decadal oscillations evident in the observations, which likely reflect the internal climate variability averaged out in the MMM. The salty spike in the IAP dataset just before 1960 is the largest departure between models and observations and even between two observation datasets (Fig. 5A). Isopycnal shifts from IAP and EN4 also show opposite directions (Fig. 5C). In addition, it is the only clear case of decadal variability in IAP and EN4 that is out of phase. Hence, this discrepancy in sea surface salinity anomalies between IAP and EN4 can be attributed to the sparsity of observations during the early period. Despite this, most estimates show outcrop salinity reaching a higher level during the 1970s and 1980s.

The impact of the two anthropogenic drivers is clearly evident in the GHG and AER runs, where both produce quasi-monotonic changes in our salinity index (Fig. 5). However, the strength of their impact varies in time: AAs (blue curve; Fig. 5) induce rapid changes during the first several decades, and an almost flat or weakly reversed response since the 1980s (figs. S9 and S10); the GHG effect (red curve; Fig. 5) is more monotonic and becomes stronger during recent decades.

To further explore the model spread of these responses, we use the piecewise trends of our salinity index calculated for each model. Despite different model water-mass geometries and the observations featuring varying density levels of the water-mass responses (Figs. 1 and 3), it is striking to find a clear intermodel relationship between dS_{outcrop} and dS_{shift} in the North Pacific (Fig. 6). With a very strong intermodel correlation ($r \geq 0.87$), dS_{shift} accounts for around 60 to 75% of dS_{outcrop} based on a linear regression (Fig. 6, A and C). Similarly, the correlation is strong between the change of

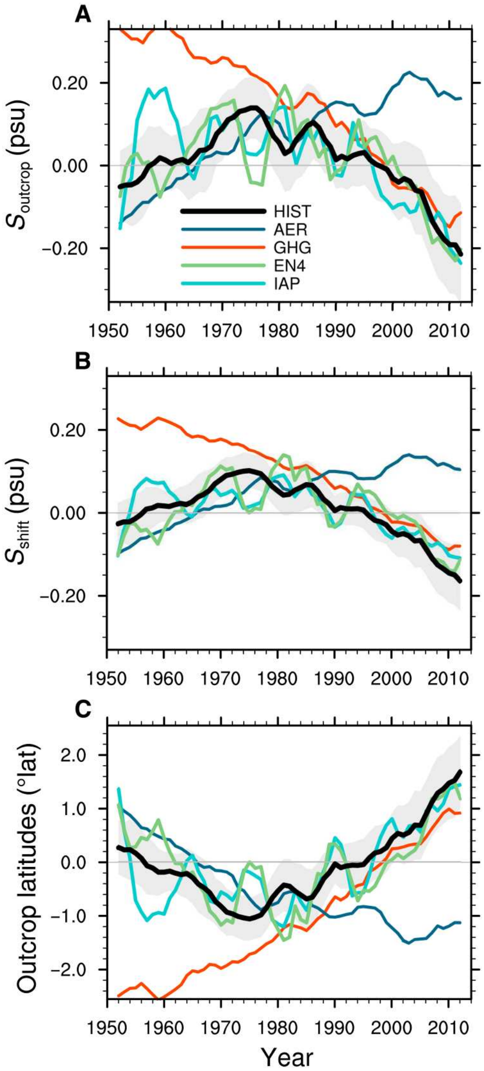

Fig. 5. Time evolutions of the salinity and latitudes of outcrops. Time series of (**A**) $S_{outcrop}$ in the North Pacific (black triangles in previous figures) from observations (EN4 as green curve and IAP as cyan curve) and CMIP6 simulations (HIST MMM shown as black curve). (**B**) S_{shift}. (**C**) Latitudes of the winter outcrops. AER result (blue curve) is relative to the 1950–1985 mean, and GHG result (red curve) is relative to the 1985–2014 mean, with the remaining curves relative to the mean of 1950–2014. Gray shading shows ±2 × the SE for HIST across 10 models at each time step.

outcrop latitudes (*dLat*) and $dS_{outcrop}$ (Fig. 6, B and D). Moreover, this intermodel spread in *dLat* is affected by the global mean surface temperature change (fig. S11), which reflects the model-dependent climate sensitivity to anthropogenic forcings. In addition, the differences in mean salinity gradient among models have little contribution to the spread of $dS_{outcrop}$ (fig. S12).

During 1950–1985, the trends from the all-forcing experiment and observations are located within the same quadrant as the results from AER runs (Fig. 6, A and B). This indicates that the AA fingerprint on water-mass change is prominent during this period. Because of the "spike" around 1960 (Fig. 5A), the IAP dataset shows a smaller change than that from EN4 dataset, but the observations generally lie on the regression line of the models.

For the three decades after 1985, the results from the HIST runs and observations are dominated by the GHG effect (Fig. 6, C and D). Moreover, there is no good agreement about the direction of change (i.e., sign of the trends) induced by AA forcing across models during this period. In other words, AAs from some models reinforce the GHG effect but offset it in others in this latter period. Clearly, the change in the sign of the trend of North Pacific water-mass variation reflects the domination of AA forcing in the earlier period and GHG forcing in the latter.

DISCUSSION

We have isolated and detected the fingerprint of AAs in subsurface water-mass changes for the first time. Our focus is the relatively well-observed North Pacific Ocean. Like the extensively studied anthropogenic signals in the ocean associated with GHG warming (*45*–*47*), AA climate forcing should have left long-lasting oceanic signals, such as the equatorward migration of isopycnal outcrops primarily due to the regional surface cooling (*14*) found in this study. We show that multidecadal interior thermocline water-mass changes (salinity changes on density surfaces) in the North Pacific can be understood in terms of this outcrop migration, which drives salinity increase at the surface outcrop around 30°N, and the resulting penetration of these changes into the ocean interior along the isopycnals via subduction. This mechanism, found before for average changes in 1950–2008 (*15*), provides a clear path for the subsurface ocean to retain detectable evidence of anthropogenic forcings. We find that salinity change due to isopycnal migration accounts for ~70% of total salinity change following outcrops in the vicinity of the salinity front in the North Pacific.

We find a clear competition between GHG forcing and AA forcing during the historical period since 1950, and their individual effects dominate the North Pacific water-mass changes during different periods. AA forcing on North Pacific thermocline water masses is dominant over the GHG effect during 1950–1985 based on model experiments with AA and GHG forcing separated, resulting in salinification in the historical all-forcing simulations, which is consistent with the observed changes. After this period, GHG impacts take over, leading to freshening on the density surfaces, again consistent with the observations. Analysis of trends of salinity following outcrops in the periods before and after 1985 across models and observations confirm this handover from one forcing type to another (cooling by AA to warming by GHG) around the subduction sites in the central North Pacific gyre. The strength of the water-mass signal is linearly related to outcrop migration strength, which in turn is controlled by the surface warming/cooling signal in the region. Overall, this nonmonotonic behavior is a clear "fingerprint" from the competition between the strength of these two anthropogenic forcings.

Our study has focused on the North Pacific largely due to its relatively rich historical observation record and predominantly zonal outcrop and water-mass structures, the former allowing detection and the latter allowing us to use zonal averages in our pattern analysis. We have looked at the modeled water-mass changes in other ocean basins, which reveal a similar story around the dominant effect of outcrop migration in the two eras examined here, although detection of these signals in those basins will require a more sophisticated approach, which will be a topic for future work.

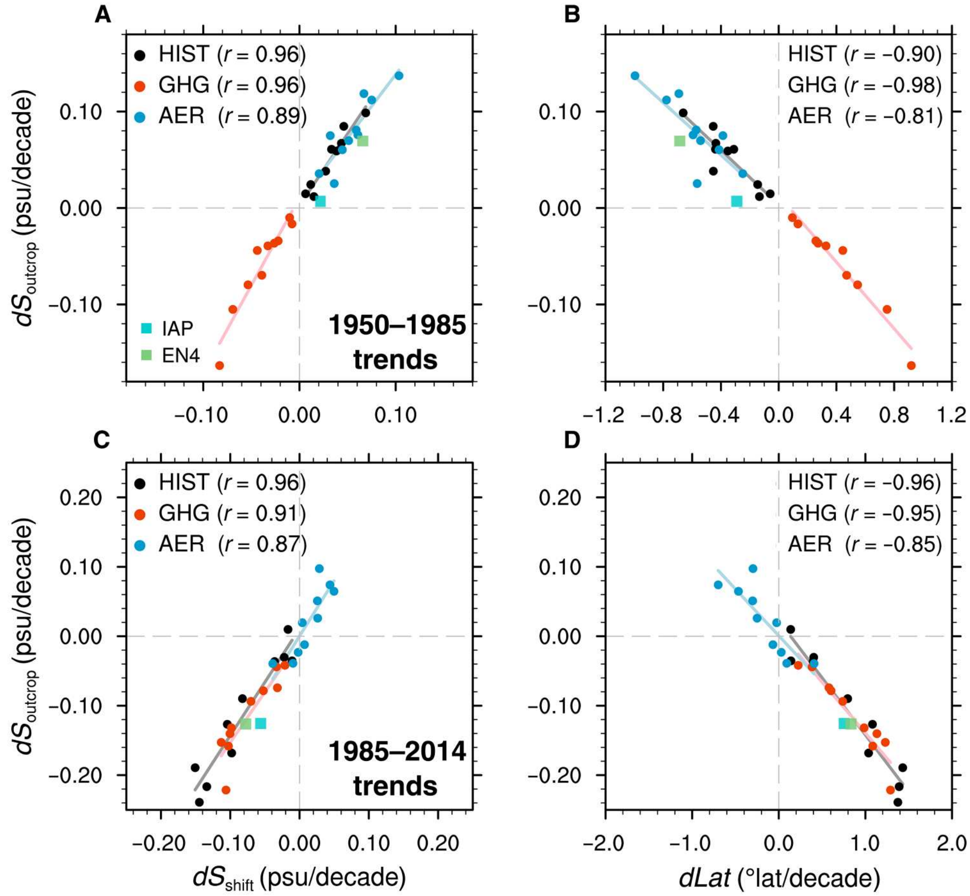

Fig. 6. Links to salinity trends and outcrop migrations. Scatterplot for dS_{outcrop} against (**A** and **C**) dS_{shift} and (**B** and **D**) the trend of the winter outcrop latitudes (*dLat*) in the North Pacific. (A) and (B) show trends during 1950–1985, and (C) and (D) show trends during 1985–2014. Each circle represents the result from each model ensemble mean. Squares are estimates from the observation products. The correlation coefficients across model runs are shown in the bracket. The linear regression line is drawn when the regression is significant at the 95% confidence level.

In our study, we have linked the GHG-induced surface warming and aerosol-induced cooling to changes at the outcrops and, subsequently, the interior ocean (via mean subduction). We have not looked in detail at what controls the detailed patterns of surface temperature change in this study. Exploring this poses interesting questions that warrant further investigation in the future.

Future projections assume that AAs will decrease substantially due to air pollution regulations and the short residence time of aerosols (*20*, *48*). This implies that AAs and GHGs will work in the same direction to create even stronger warming and thus water-mass changes. This will certainly extend beyond the North Pacific Ocean. With a better global ocean observation network in place, we expect that warming-driven water-mass changes will continue to intensify and penetrate larger volumes of the global ocean.

MATERIALS AND METHODS

Observational datasets

Temperature and salinity from EN4 and IAP datasets were used to examine the water-mass trends since 1950. EN4 (version EN4.2.2) is an observation-based gridded dataset from the Met Office Hadley Centre for the subsurface properties for global oceans with monthly resolution (*40*). The bathythermograph bias was corrected using the methods from (*49*, *50*). The data are on a regular 1° × 1° latitude-longitude grid with 42 vertical depth levels in the upper 2000 m. The IAP dataset from the Institute of Atmospheric Physics provides monthly mean ocean temperature and salinity starting from 1940 (*41*). The data are on a regular 1° × 1° grid with 41 vertical depth levels in the upper 2000 m. We investigate the period of 1950–2014 to compare with the historical simulations from the CMIP6 models.

For the surface air temperature (the temperature at a height of 2 m), we used the ERA5 global reanalysis data and its back extension, which reaches back to 1950 (*51*). Global mean surface temperature (GMST) is calculated by averaging surface air temperature.

CMIP6 experiments and models

In this study, we mainly used three CMIP6 experiments: the historical all-forcing experiment (HIST), the greenhouse gas single-forcing experiment (GHG), and the anthropogenic aerosol single-forcing experiment (AER) (*52*, *53*). HIST runs aim to reproduce observed climate change and include realistic external forcing from GHGs, AAs, insolation, ozone depletion, volcano eruption, and land-use change. To better understand the effect of major anthropogenic forcing agents, GHGs and AAs are the only time-varying forcing agent with other terms fixed at the preindustrial level in GHG and AER runs, respectively. Each experiment covers the period from 1850 to 2014. We analyzed the period since 1950 to compare simulations with observations. The turning point to calculate the piecewise trends is chosen as year 1985. The results are insensitive when the turning point is chosen within the 1980s. In addition, the preindustrial (piControl) runs, to which no external forcing is applied, were also used to obtain the subsurface drifts of water mass from models, which should be removed from HIST, GHG, and AER runs (see below).

We used 10 CMIP6 models that performed all of the aforementioned experiments. Each model has several ensemble members, forced by the same external forcing, but exhibits different internal climate variability. The number of ensemble members for each model is listed in table S1. The ensemble mean was calculated to remove the internal variability to some extent from each model and largely reflects the responses driven by external forcing. We interpolated all the outputs from models to a regular 1° × 1° grid.

Water-mass changes

Potential density was calculated using potential temperature and salinity fields from two observed datasets and all CMIP6 simulations (*54*). σ_1 (potential density referenced to 1000 dbar) was used to more accurately represent the observed water-mass change within the upper 2000 m. All gridded fields were then linearly interpolated onto density (σ_1 = 26–32.3 kg m^{-3}) levels. The salinity and temperature exhibit the anomalies with the same structure and opposite signs when they were examined on the density coordinate. In this study, we use salinity change in density space to represent the water-mass change.

The salinity change at the maximum winter (March for Northern Hemisphere and September for Southern Hemisphere used here) outcrop (where σ_1 reaches the surface), of which the latitudes change over time, can be decomposed into several terms (*15*)

$$\frac{dS}{dt}\Big|_{\sigma_1,x} \approx \frac{d\overline{S}}{dy}\frac{dy}{dt}\Big|_{\sigma_1,x} + \frac{dS'}{dt}\Big|_{\sigma_1,x} \quad (1)$$

where x and y are longitude and latitude of the outcrops, $\overline{S}$ is the climatological mean salinity for 1950–2014, S' is the temporal perturbation, and total salinity is defined as $S = \overline{S} + S'$. The first right-hand-side (rhs) terms in Eq. 1 are salinity changes at the outcrop due to a meridional shift of the outcrop. The second rhs term is the temporal change of the surface salinity field, likely due to freshwater flux changes, at time-varying outcrop. In this study, we focused on the contribution of the change due to a meridional shift (first rhs term, hereafter dS_{shift}) and found that it plays the leading role in the total water-mass change at the outcrop (left-hand-side term, hereafter dS_{outcrop}) and further affects the subsurface water masses. For presentation, these salinity changes, i.e., dS_{outcrop} and dS_{shift}, at the outcrops are used to calculate zonal mean along the outcrops for the Pacific basin. In this study, we focus on the North Pacific water-mass change, but the South Pacific responses are also shown for completeness.

The change associated with a meridional shift can be further decomposed into two parts. One is the meridional gradients in the mean salinity filed, $\frac{d\overline{S}}{dy}\big|_{\sigma_1,x}$. The other is the meridional shift of the outcrop, $\frac{dy}{dt}\big|_{\sigma_1,x}$ (*dLat* in the main text and figures), which is sensitive to surface temperature change (*10*). We further investigated and quantified the contribution of these two components to dS_{outcrop} and the associated intermodel spread.

Model drift removal

Coupled climate models are prone to long-term drift, which can contaminate the detection of long-term trends driven by external forcing. After the outputs from piControl run from each model were converted to the density coordinate, we estimated the drift of salinity in density space at each grid point by fitting a cubic polynomial. Realizations in the forced experiments branch out from piControl run at different times. Using the branch time information (the time when forced experiments branch out) provided in the file metadata, the correct segment of the cubic polynomial from piControl was subtracted from the forced simulation. After removing the drift, we conducted the ensemble mean and zonal mean in the Pacific basin, and finally calculated the trends for certain periods, i.e., 1950–1985 and 1985–2014.

Supplementary Materials

This PDF file includes:
Table S1
Figs. S1 to S12

REFERENCES AND NOTES

1. M. R. Allen, W. J. Ingram, Constraints on future changes in climate and the hydrologic cycle. *Nature* **419**, 224–232 (2002).
2. I. M. Held, B. J. Soden, Robust responses of the hydrological cycle to global warming. *J. Climate* **19**, 5686–5699 (2006).
3. F. J. Wentz, L. Ricciardulli, K. Hilburn, C. Mears, How much more rain will global warming bring? *Science* **317**, 233–235 (2007).
4. K. E. Trenberth, L. Smith, T. Qian, A. Dai, J. Fasullo, Estimates of the global water budget and its annual cycle using observational and model data. *J. Hydrometeorol.* **8**, 758–769 (2007).
5. K. Trenberth, Changes in precipitation with climate change. *Climate Res.* **47**, 123–138 (2011).
6. R. P. Allan, C. Liu, M. Zahn, D. A. Lavers, E. Koukouvagias, A. Bodas-Salcedo, Physically consistent responses of the global atmospheric hydrological cycle in models and observations. *Surv. Geophys.* **35**, 533–552 (2014).
7. N. L. Bindoff, J. Willebrand, V. Artale, A. Cazenave, J. Gregory, S. Gulev, K. Hanawa, C. Le Quéré, S. Levitus, Y. Nojiri, C. K. Shum, L. D. Talley, A. Unnikrishnan, Observations: Oceanic climate change and sea level, in *Climate Change 2007: The Physical Science Basis*. Contribution of Working Group I to the Fourth Assessment Report of the Intergovernmental Panel on Climate Change, S. Solomon, D. Qin, M. Manning, Z. Chen, M. Marquis, K. B. Averyt, M. Tignor, H. L. Miller, Eds. (Cambridge Univ. Press, 2007).
8. L. D. Talley, Freshwater transport estimates and the global overturning circulation: Shallow, deep and throughflow components. *Prog. Oceanogr.* **78**, 257–303 (2008).
9. P. J. Durack, S. E. Wijffels, R. J. Matear, Ocean salinities reveal strong global water cycle intensification during 1950 to 2000. *Science* **336**, 455–458 (2012).
10. N. Skliris, J. D. Zika, G. Nurser, S. A. Josey, R. Marsh, Global water cycle amplifying at less than the Clausius-Clapeyron rate. *Sci. Rep.* **6**, 38752 (2016).
11. N. T. Vinogradova, R. M. Ponte, In search of fingerprints of the recent intensification of the ocean water cycle. *J. Climate* **30**, 5513–5528 (2017).
12. J. D. Zika, N. Skliris, A. T. Blaker, R. Marsh, A. J. G. Nurser, S. A. Josey, Improved estimates of water cycle change from ocean salinity: The key role of ocean warming. *Environ. Res. Lett.* **13**, aace42 (2018).
13. L. Cheng, K. E. Trenberth, N. Gruber, J. P. Abraham, J. T. Fasullo, G. Li, M. E. Mann, X. Zhao, J. Zhu, Improved estimates of changes in upper ocean salinity and the hydrological cycle. *J. Climate* **33**, 10357–10381 (2020).
14. V. Lago, S. E. Wijffels, P. J. Durack, J. A. Church, N. L. Bindoff, S. J. Marsland, Simulating the role of surface forcing on observed multidecadal upper-ocean salinity changes. *J. Climate* **29**, 5575–5588 (2016).
15. P. J. Durack, S. E. Wijffels, Fifty-year trends in global ocean salinities and their relationship to broad-scale warming. *J. Climate* **23**, 4342–4362 (2010).

16. G. Myhre, D. Shindell, F.-M. Bréon, W. Collins, J. Fuglestvedt, J. Huang, D. Koch, J.-F. Lamarque, D. Lee, B. Mendoza, T. Nakajima, A. Robock, G. Stephens, T. Takemura, H. Zhang, Anthropogenic and natural radiative forcing, in *Climate Change 2013—The Physical Science Basis. Contribution of Working Group I to the Fifth Assessment Report of the Intergovernmental Panel on Climate Change* (Cambridge Univ. Press, 2013), pp. 659–740.
17. O. O. Boucher, G. Claire, C. Hoose, A. Jones, Clouds and Aerosols, in *Climate Change 2013—The Physical Science Basis*, Intergovernmental Panel on Climate Change, Ed. (Cambridge Univ. Press, 2013), pp. 571–658.
18. D. T. Shindell, G. Faluvegi, L. Rotstayn, G. Milly, Spatial patterns of radiative forcing and surface temperature response. *J. Geophys. Res. Atmos.* **120**, 5385–5403 (2015).
19. S.-P. Xie, B. Lu, B. Xiang, Similar spatial patterns of climate responses to aerosol and greenhouse gas changes. *Nat. Geosci.* **6**, 828–832 (2013).
20. J.-R. Shi, S.-P. Xie, L. D. Talley, Evolving relative importance of the Southern Ocean and North Atlantic in anthropogenic ocean heat uptake. *J. Climate* **31**, 7459–7479 (2018).
21. C. Deser, A. S. Phillips, I. R. Simpson, N. Rosenbloom, D. Coleman, F. Lehner, A. G. Pendergrass, P. Dinezio, S. Stevenson, Isolating the evolving contributions of anthropogenic aerosols and greenhouse gases: A new CESM1 large ensemble community resource. *J. Climate* **33**, 7835–7858 (2020).
22. J. T. Fasullo, P. R. Gent, R. S. Nerem, Sea level rise in the CESM large ensemble: The role of individual climate forcings and consequences for the coming decades. *J. Climate* **33**, 6911–6927 (2020).
23. M. Rhein, S. R. Rintoul, S. Aoki, E. Campos, D. Chambers, R. A. Feely, S. Gulev, G. C. Johnson, S. A. Josey, A. Kostianoy, C. Mauritzen, D. Roemmich, L. D. Talley, F. Wang, Observations: Ocean, in *Climate Change 2013—The Physical Science Basis*, Intergovernmental Panel on Climate Change, Ed. (Cambridge Univ. Press, 2014), pp. 255–316.
24. K. E. Trenberth, J. T. Fasullo, M. A. Balmaseda, Earth's energy imbalance. *J. Climate* **27**, 3129–3144 (2014).
25. P. A. Stott, S. F. B. Tett, G. S. Jones, M. R. Allen, J. F. B. Mitchell, G. J. Jenkins, External control of 20th century temperature by natural and anthropogenic forcings. *Science* **290**, 2133–2137 (2000).
26. D. M. Smith, B. B. B. Booth, N. J. Dunstone, R. Eade, L. Hermanson, G. S. Jones, A. A. Scaife, K. L. Sheen, V. Thompson, Role of volcanic and anthropogenic aerosols in the recent global surface warming slowdown. *Nat. Clim. Chang.* **6**, 936–940 (2016).
27. Y. Hwang, D. M. W. Frierson, S. M. Kang, Anthropogenic sulfate aerosol and the southward shift of tropical precipitation in the late 20th century. *Geophys. Res. Lett.* **40**, 2845–2850 (2013).
28. H. Wang, S. P. Xie, Q. Liu, Comparison of climate response to anthropogenic aerosol versus greenhouse gas forcing: Distinct patterns. *J. Climate* **29**, 5175–5188 (2016).
29. A. Giannini, A. Kaplan, The role of aerosols and greenhouse gases in Sahel drought and recovery. *Clim. Change* **152**, 449–466 (2019).
30. C. Takahashi, M. Watanabe, Pacific trade winds accelerated by aerosol forcing over the past two decades. *Nat. Clim. Chang.* **6**, 768–772 (2016).
31. C. J. W. Bonfils, B. D. Santer, J. C. Fyfe, K. Marvel, T. J. Phillips, S. R. H. Zimmerman, Human influence on joint changes in temperature, rainfall and continental aridity. *Nat. Clim. Chang.* **10**, 726–731 (2020).
32. W. J. Dow, A. C. Maycock, M. Lofverstrom, C. J. Smith, The effect of anthropogenic aerosols on the aleutian low. *J. Climate* **34**, 1725–1741 (2021).
33. A. J. Dittus, E. Hawkins, J. I. Robson, D. M. Smith, L. J. Wilcox, Drivers of recent North Pacific decadal variability: The role of aerosol forcing. *Earth's Futur.* **9**, 1–14 (2021).
34. C. Diao, Y. Xu, S. Xie, Anthropogenic aerosol effects on tropospheric circulation and sea surface temperature (1980–2020): Separating the role of zonally asymmetric forcings. *Atmos. Chem. Phys.* **21**, 18499–18518 (2021).
35. S. M. Kang, S. Xie, C. Deser, B. Xiang, Zonal mean and shift modes of historical climate response to evolving aerosol distribution. *Sci. Bull.* **66**, 2405–2411 (2021).
36. J.-R. Shi, Y.-O. Kwon, S. E. Wijffels, Two distinct modes of climate responses to the anthropogenic aerosol forcing changes. *J. Climate* **35**, 3445–3457 (2022).
37. J.-R. Shi, Y. Kwon, S. E. Wijffels, Subsurface ccean temperature responses to the anthropogenic aerosol forcing in the North Pacific. *Geophys. Res. Lett.* **50**, 1–16 (2023).
38. N. L. Bindoff, T. J. Mcdougall, Diagnosing climate change and ocean ventilation using hydrographic data. *J. Phys. Oceanogr.* **24**, 1137–1152 (1994).
39. K. Lyu, X. Zhang, J. A. Church, Q. Wu, Processes responsible for the southern hemisphere ocean heat uptake and redistribution under anthropogenic warming. *J. Climate* **33**, 3787–3807 (2020).
40. S. A. Good, M. J. Martin, N. A. Rayner, EN4: Quality controlled ocean temperature and salinity profiles and monthly objective analyses with uncertainty estimates. *J. Geophys. Res. Ocean.* **118**, 6704–6716 (2013).
41. L. Cheng, G. Wang, J. Abraham, G. Huang, Decadal ocean heat redistribution since the late 1990s and its association with key climate modes. *Climate* **6**, 91 (2018).
42. T. Suga, K. Motoki, Y. Aoki, A. M. MacDonald, The North Pacific climatology of winter mixed layer and mode waters. *J. Phys. Oceanogr.* **34**, 3–22 (2004).
43. J. R. Luyten, J. Pedlosky, H. Stommel, The ventilated thermocline. *J. Phys. Oceanogr.* **13**, 292–309 (1983).
44. L. D. Talley, Ventilation of the subtropical North Pacific: The shallow salinity minimum. *J. Phys. Oceanogr.* **15**, 633–649 (1985).
45. T. P. Barnett, D. W. Pierce, R. Schnur, Detection of anthropogenic climate change in the world's oceans. *Science* **292**, 270–274 (2001).
46. T. P. Barnett, D. W. Pierce, K. M. AchutaRao, P. J. Gleckler, B. D. Santer, J. M. Gregory, W. M. Washington, Penetration of human-induced warming into the world's oceans. *Science* **309**, 284–287 (2005).
47. P. J. Gleckler, B. D. Santer, C. M. Domingues, D. W. Pierce, T. P. Barnett, J. A. Church, K. E. Taylor, K. M. Achutarao, T. P. Boyer, M. Ishii, P. M. Caldwell, Human-induced global ocean warming on multidecadal timescales. *Nat. Clim. Chang.* **2**, 524–529 (2012).
48. D. M. Westervelt, L. W. Horowitz, V. Naik, J. C. Golaz, D. L. Mauzerall, Radiative forcing and climate response to projected 21st century aerosol decreases. *Atmos. Chem. Phys.* **15**, 12681–12703 (2015).
49. V. Gouretski, F. Reseghetti, On depth and temperature biases in bathythermograph data: Development of a new correction scheme based on analysis of a global ocean database. *Deep. Res. Part I Oceanogr. Res. Pap.* **57**, 812–833 (2010).
50. V. Gouretski, L. Cheng, Correction for systematic errors in the global dataset of temperature profiles from mechanical bathythermographs. *J. Atmos. Oceanic Tech.* **37**, 841–855 (2020).
51. H. Hersbach, B. Bell, P. Berrisford, S. Hirahara, A. Horányi, J. Muñoz-Sabater, J. Nicolas, C. Peubey, R. Radu, D. Schepers, A. Simmons, C. Soci, S. Abdalla, X. Abellan, G. Balsamo, P. Bechtold, G. Biavati, J. Bidlot, M. Bonavita, G. Chiara, P. Dahlgren, D. Dee, M. Diamantakis, R. Dragani, J. Flemming, R. Forbes, M. Fuentes, A. Geer, L. Haimberger, S. Healy, R. J. Hogan, E. Hólm, M. Janisková, S. Keeley, P. Laloyaux, P. Lopez, C. Lupu, G. Radnoti, P. Rosnay, I. Rozum, F. Vamborg, S. Villaume, J. Thépaut, The ERA5 global reanalysis. *Q. J. R. Meteorol. Soc.* **146**, 1999–2049 (2020).
52. V. Eyring, S. Bony, G. A. Meehl, C. A. Senior, B. Stevens, R. J. Stouffer, K. E. Taylor, Overview of the Coupled Model Intercomparison Project Phase 6 (CMIP6) experimental design and organization. *Geosci. Model Dev.* **9**, 1937–1958 (2016).
53. N. P. Gillett, H. Shiogama, B. Funke, G. Hegerl, R. Knutti, K. Matthes, B. D. Santer, D. Stone, C. Tebaldi, The Detection and Attribution Model Intercomparison Project (DAMIP v1.0) contribution to CMIP6. *Geosci. Model Dev.* **9**, 3685–3697 (2016).
54. T. J. McDougall, D. R. Jackett, D. G. Wright, R. Feistel, Accurate and computationally efficient algorithms for potential temperature and density of seawater. *J. Atmos. Oceanic Tech.* **20**, 730–741 (2003).

Acknowledgments: We acknowledge the World Climate Research Programme's Working Group on Coupled Modeling, which led the design of CMIP6 and coordinated the work, and we also thank individual climate modeling groups (listed in table S1) for their efforts in model simulations and projections. **Funding:** J.-R.S., S.E.W., and Y.-O.K. are supported by U.S. National Science Foundation grant OCE-2048336. L.D.T. and S.T.G. are supported by U.S. National Science Foundation grant OPP-1936222. **Author contributions:** J.-R.S., S.E.W., and Y.-O.K. conceived the study and developed the conceptual framework. J.-R.S. conducted the analysis and wrote the first draft. J.-R.S., S.E.W., Y.-O.K., L.D.T., and S.T.G. contributed to interpreting the results, writing and editing the manuscript. **Competing interests:** The authors declare that they have no competing interests. **Data and materials availability:** The CMIP6 historical and single-forcing simulation outputs are available on the Program for Climate Model Diagnostics and Intercomparison's Earth System Grid (https://esgf-node.llnl.gov/search/cmip6/). IAP data are available at https://climatedataguide.ucar.edu/climate-data/ocean-temperature-analysis-and-heat-content-estimate-institute-atmospheric-physics. EN4 data are available at https://metoffice.gov.uk/hadobs/en4/. All data needed to evaluate the conclusions in the paper are present in the paper and/or the Supplementary Materials.

Submitted 13 March 2023
Accepted 18 August 2023
Published 20 September 2023
10.1126/sciadv.adh7746

Science Advances

The competition between anthropogenic aerosol and greenhouse gas climate forcing is revealed by North Pacific water-mass changes

Jia-Rui Shi, Susan E. Wijffels, Young-Oh Kwon, Lynne D. Talley, and Sarah T. Gille

Sci. Adv., **9** (38), eadh7746.
DOI: 10.1126/sciadv.adh7746

Science Advances
AAAS

Supplementary Materials for

The competition between anthropogenic aerosol and greenhouse gas climate forcing is revealed by North Pacific water-mass changes

Jia-Rui Shi *et al.*

Corresponding author: Jia-Rui Shi, jshi@whoi.edu

Sci. Adv. **9**, eadh7746 (2023)
DOI: 10.1126/sciadv.adh7746

This PDF file includes:

Table S1
Figs. S1 to S12

Table S1. CMIP6 models and the number of realizations used in this study. The left column shows the names of 10 CMIP6 models, in which all three of the HIST, AER, and GHG runs are available. The right column shows the number of realizations in these externally-forced runs for each model. The realizations used are shown in the bracket.

Model Names	Number of Realizations used in HIST, AER, and GHG
ACCESS-CM2	3 (r1-r3)
ACCESS-ESM1-5	3 (r1-r3)
CanESM5	15 (r1-15)
CESM2	2 (r1 and r3)
CNRM-CM6-1	3 (r1-r3)
HadGEM3-GC31-LL	4 (r1-r4)
IPSL-CM6A-LR	10 (r1-r3)
MIROC6	3 (r1-r3)
MRI-ESM2-0	5 (r1-r3)
NorESM2-LM	3 (r1-r3)

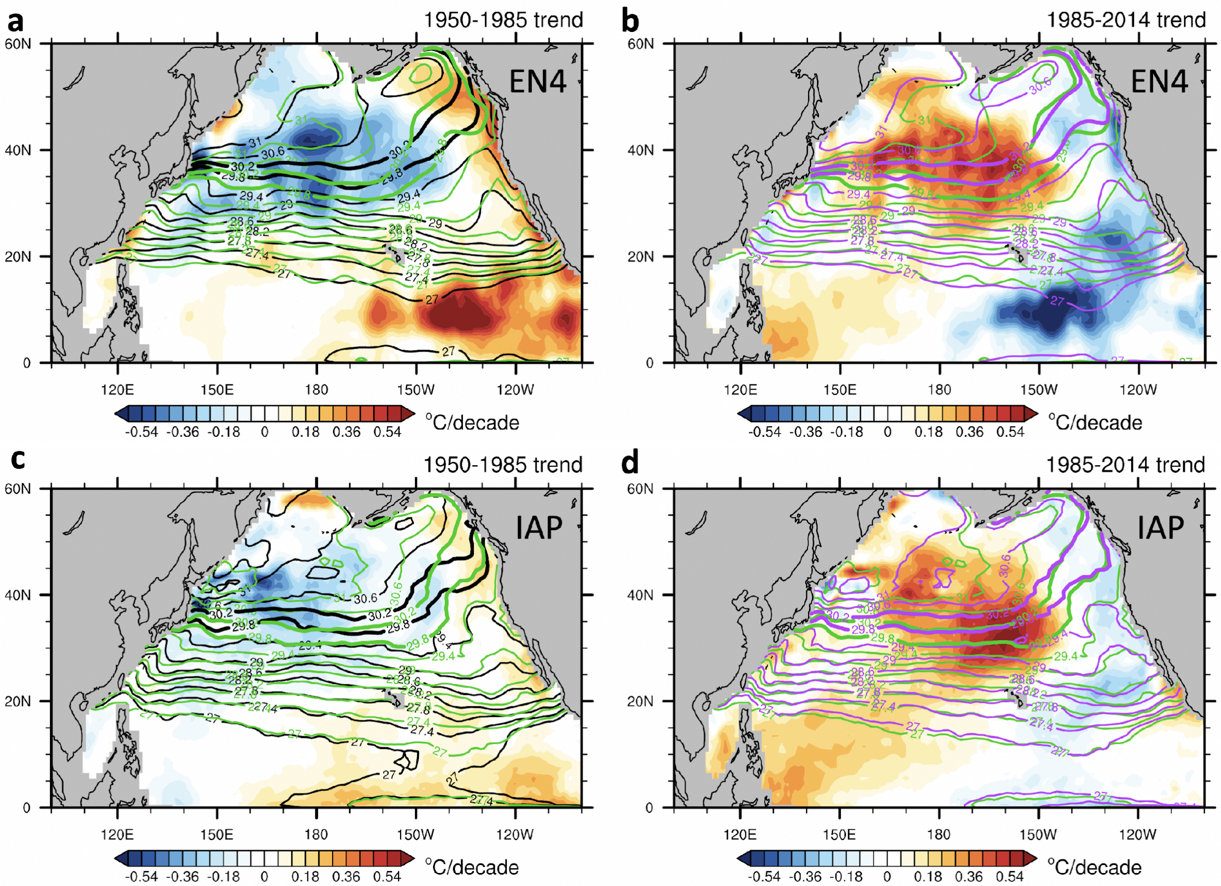

Fig. S1. North Pacific winter sea surface temperature trends for different periods from EN4 (**a,b**) and IAP (**c,d**). Black contours are 1950-1954 mean winter σ_1 at the sea surface (outcrops). Green contours are 1983-1987 mean outcrops. Purple ones are 2010-2014 mean outcrops. The thicker contours indicate the outcrop locations for σ_1 =29.8 and 30.2.

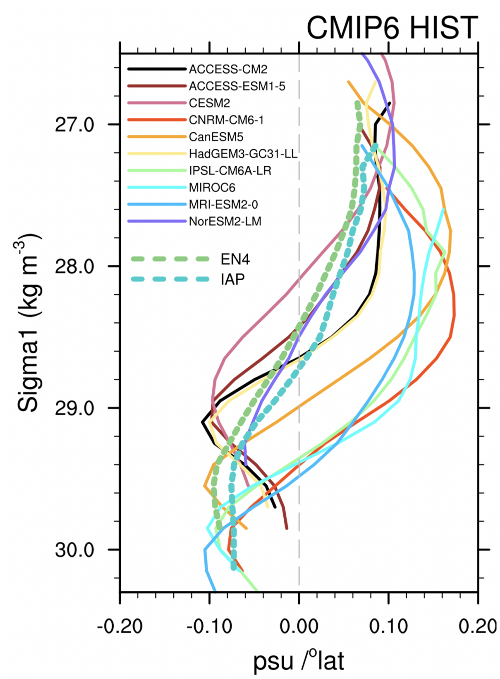

Fig. S2. Zonal mean climatological meridional salinity gradient at the winter surface outcrops in the North Pacific from observations (dashed curves) and CMIP6 models. The zonal mean is calculated along each outcrop.

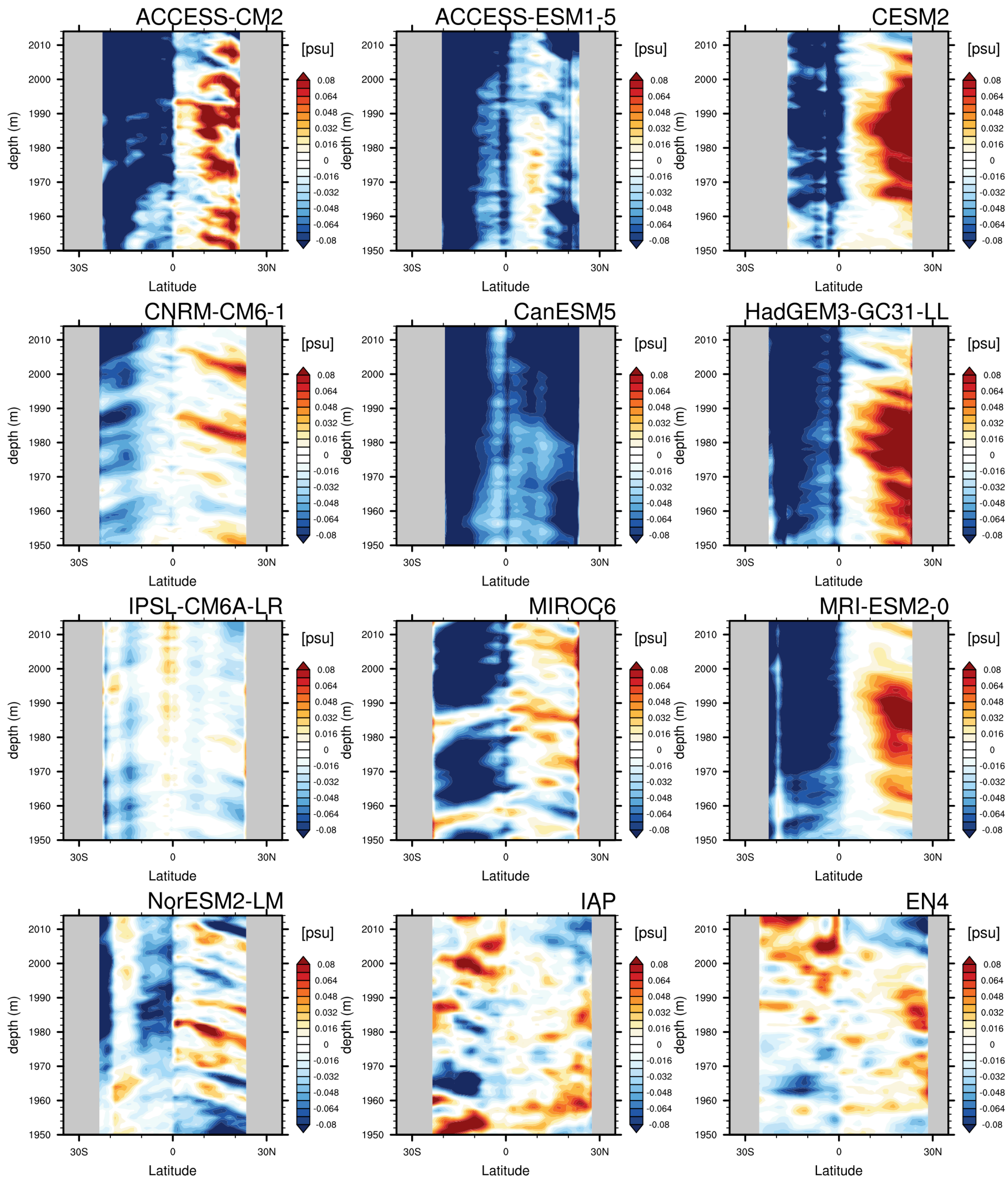

Fig. S3. Hovmöller diagrams of the salinity anomalies at the salinity front in the North Pacific from CMIP6 HIST runs and observations.

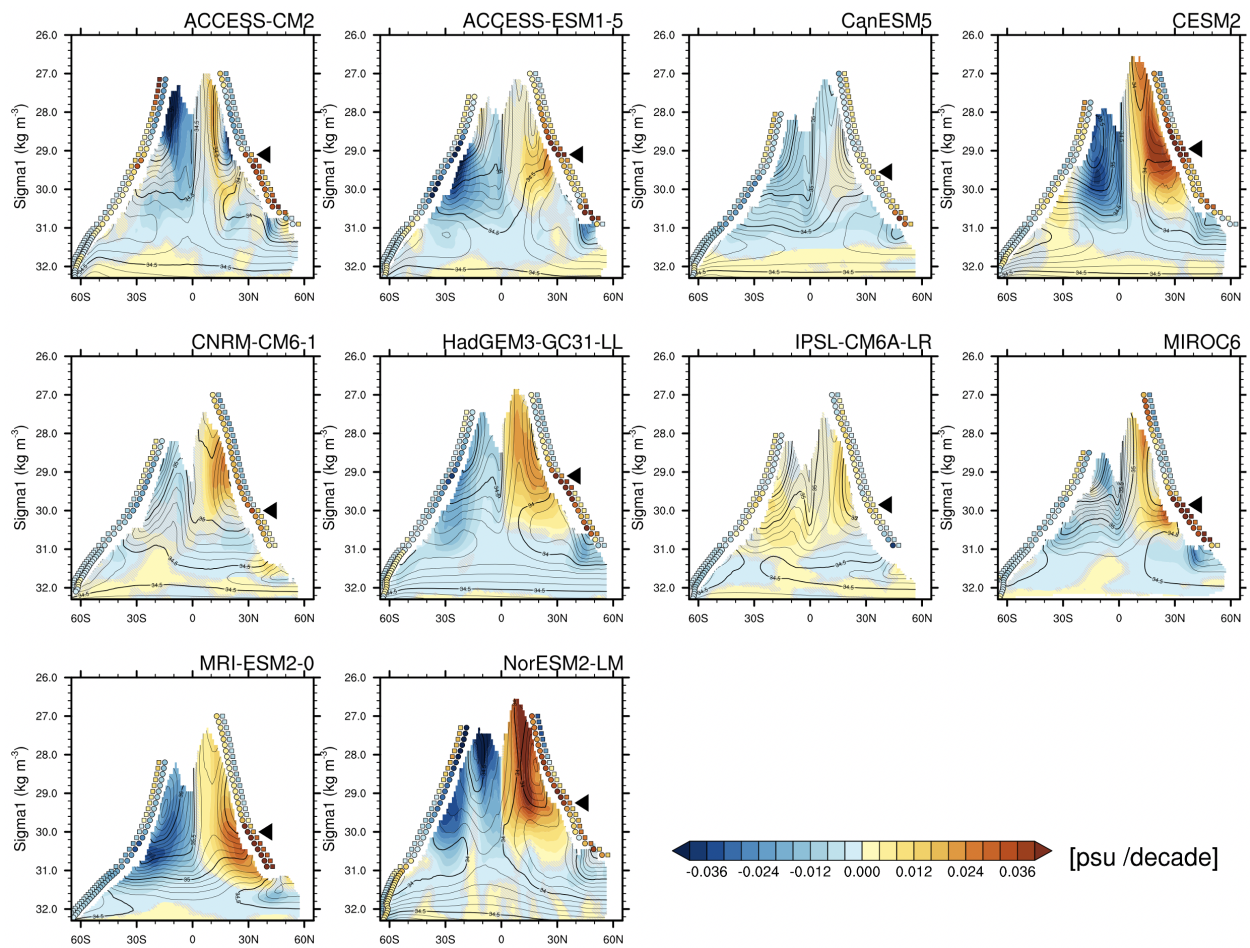

Fig. S4. As in Fig. 3, but for 1950-1985 trends from HIST runs.

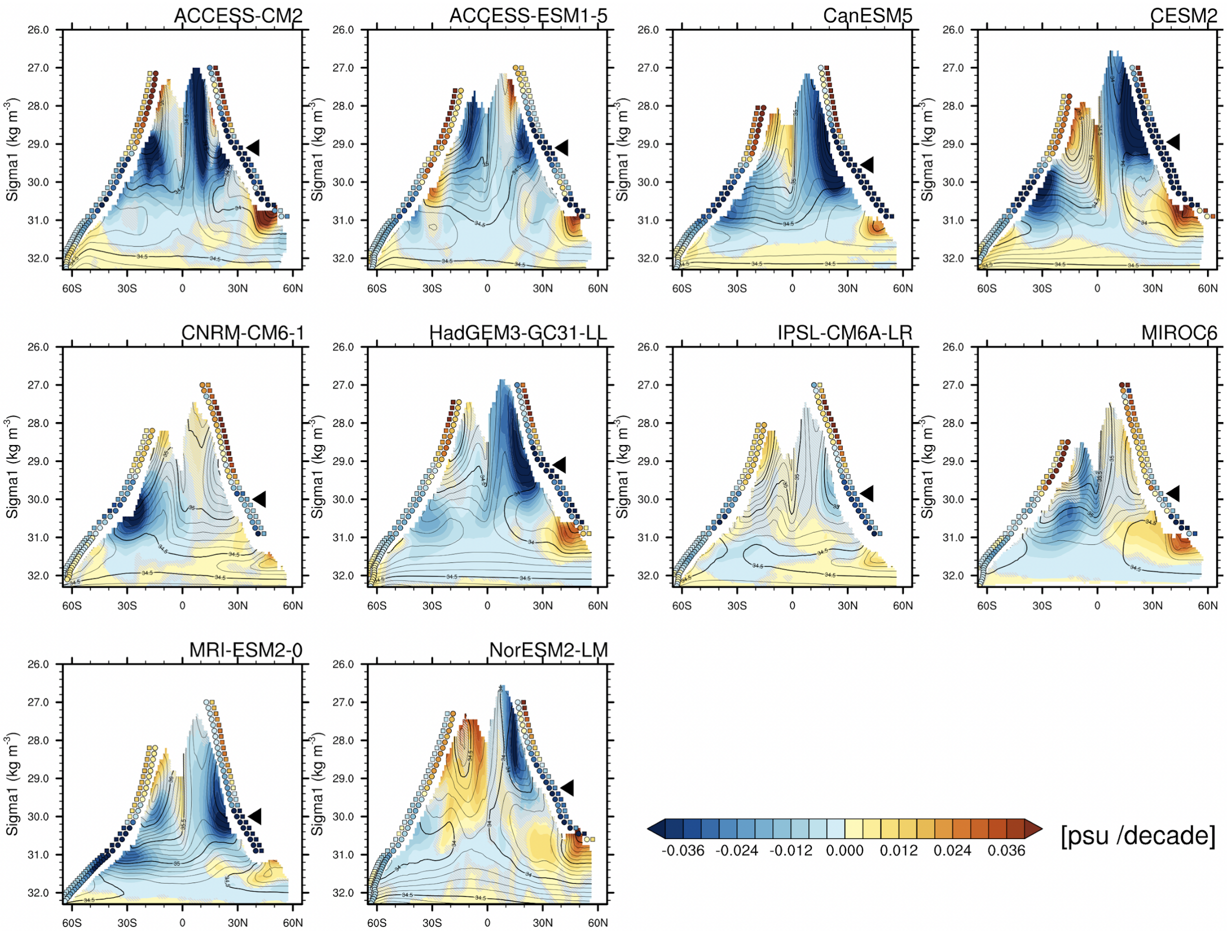

Fig. S5. As in Fig. 3, but for 1985-2014 trends from HIST runs.

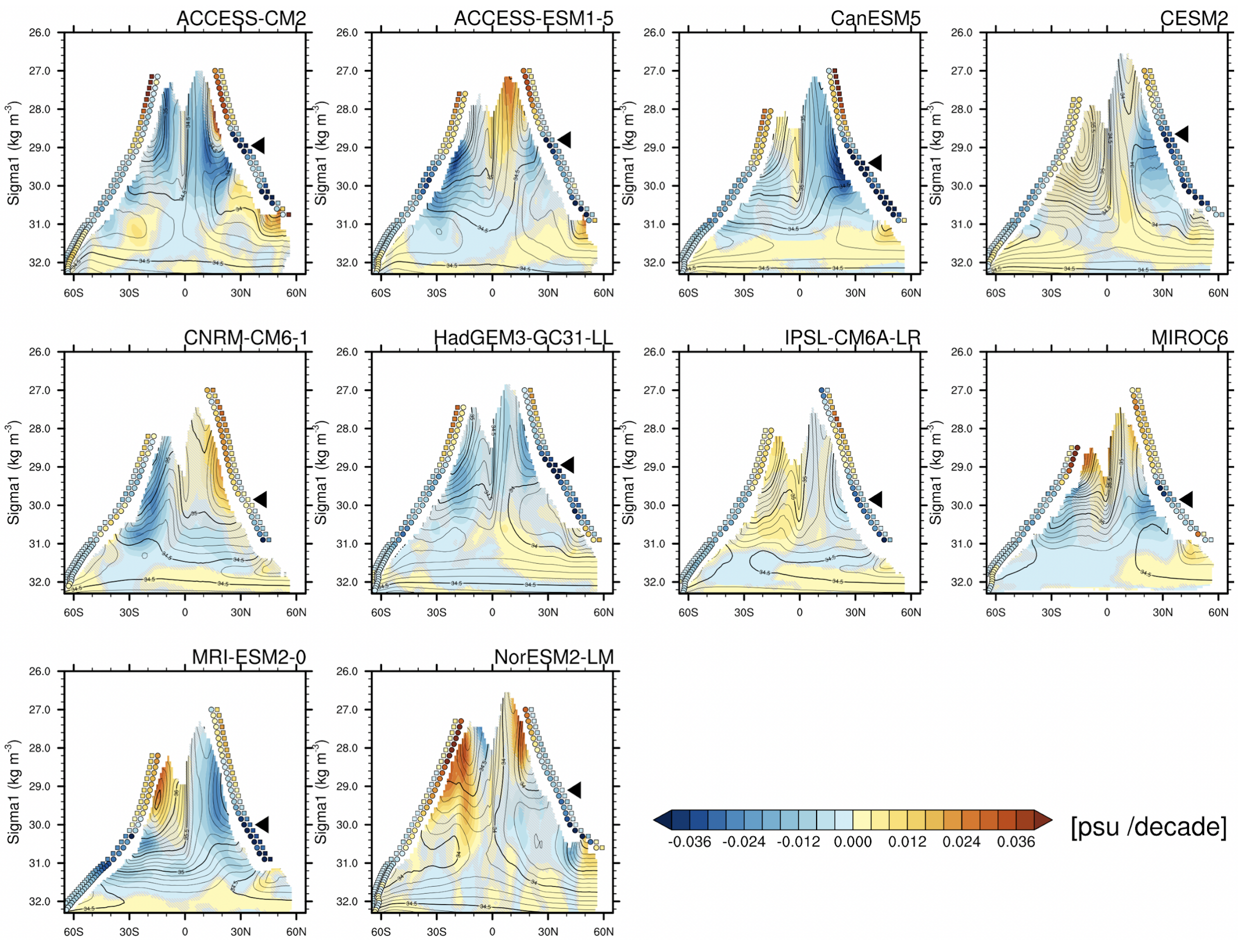

Fig. S6. As in Fig. 3, but for 1950-1985 trends from GHG runs.

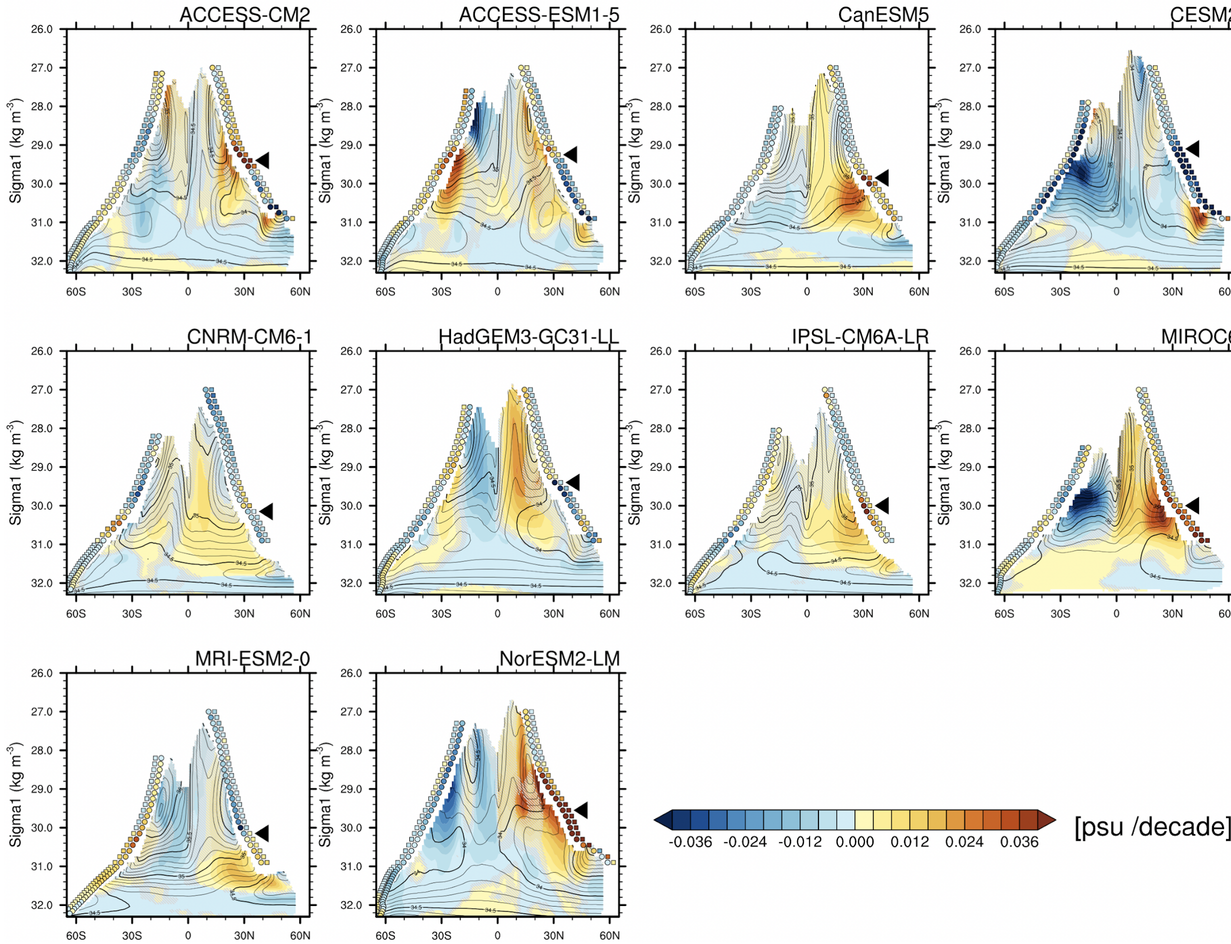

Fig. S7. As in Fig. 3, but for 1985-2014 trends from AER runs.

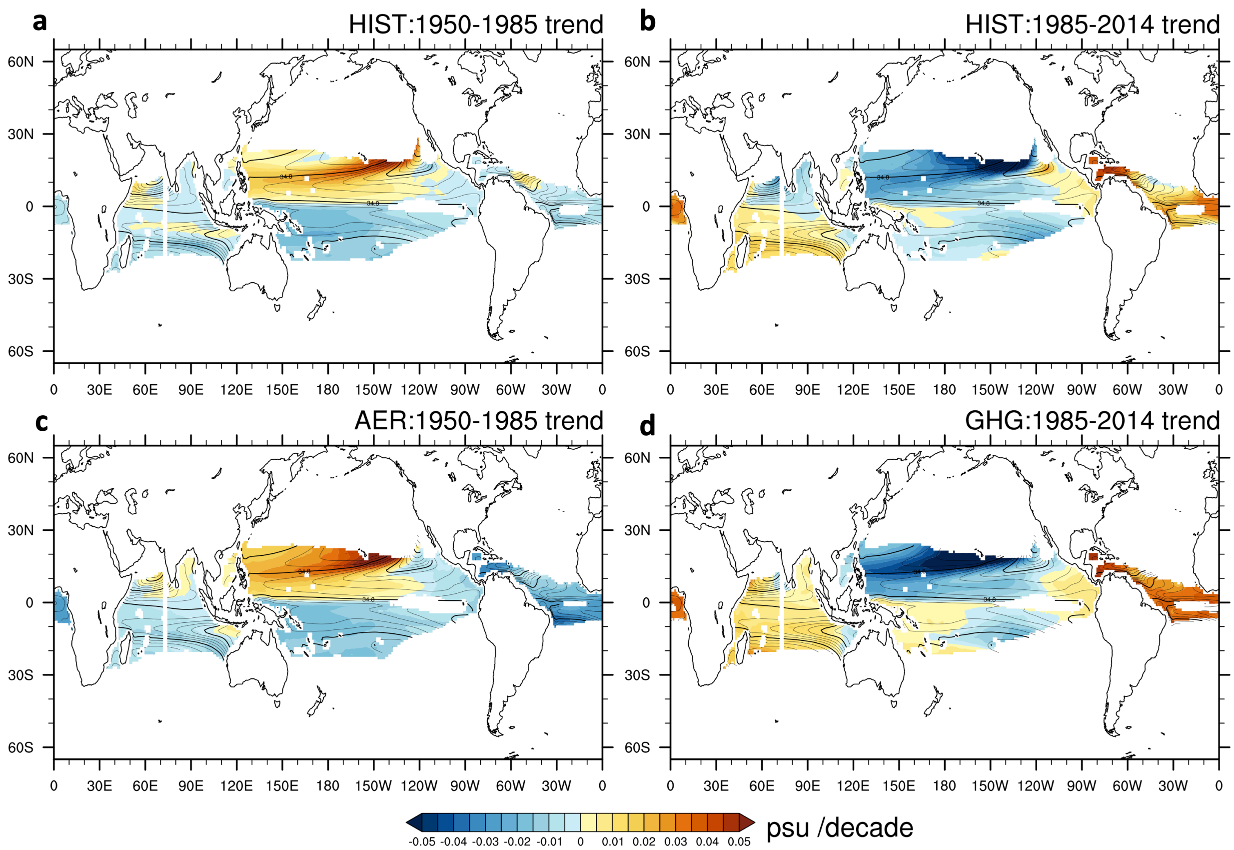

Fig. S8. Salinity trends at the North Pacific salinity front from CMIP6 experiments: (**a-b**) trends from HIST MMM for the periods 1950-1985 and 1985-2014 (**c**) trends from AER MMM for the period 1950-1985, and (**d**) trend from GHG MMM for the period 1985-2014. Climatological annual mean salinity is shown as black contours.

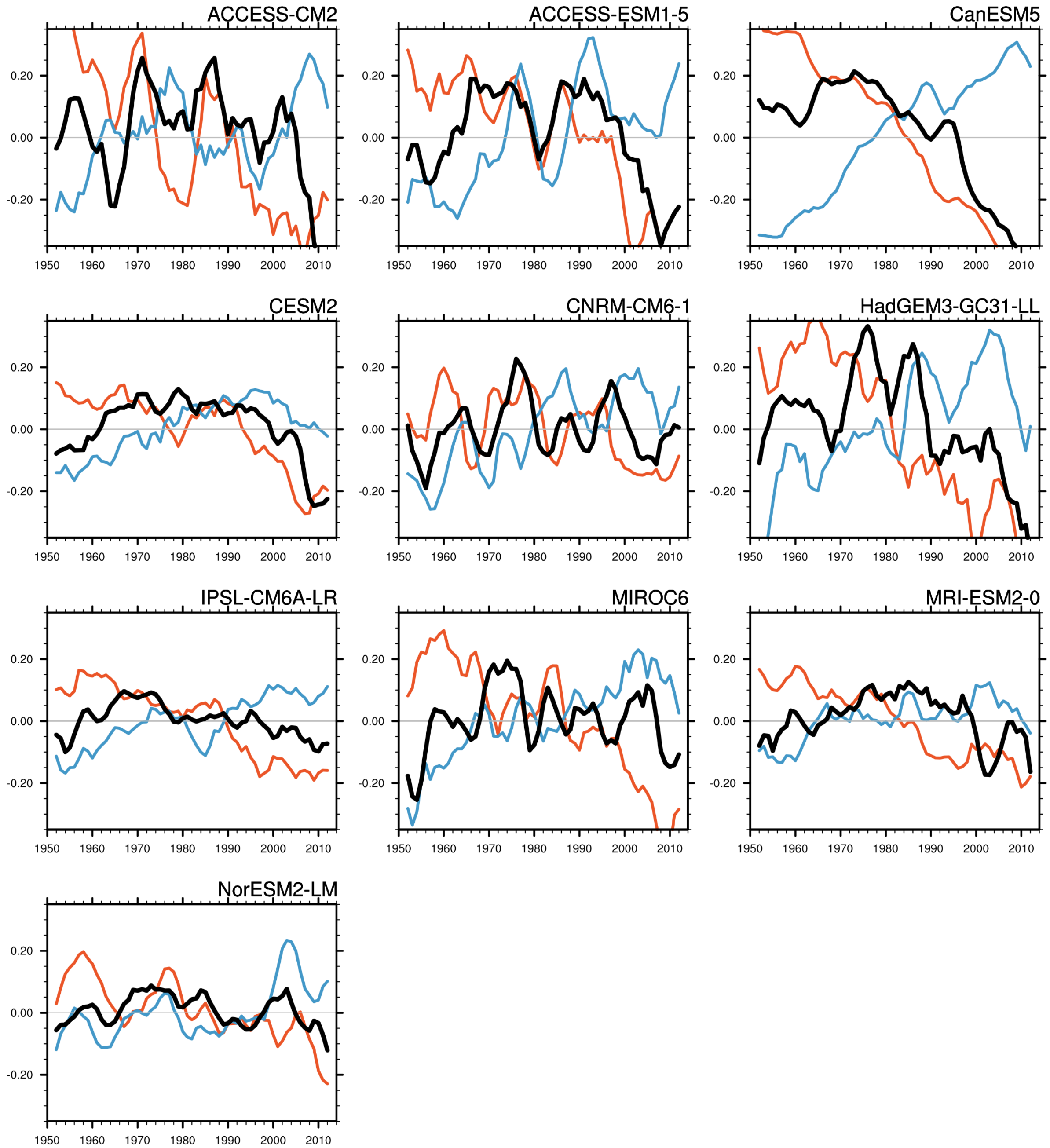

Fig. S9. Time series of surface salinity anomalies (in psu) at the surface salinity front ($S_{outcrop}$) in the North Pacific from CMIP6 models. Ensemble means for HIST, GHG, and AER are shown as black, red, and blue curves, respectively. All curves are relative to the 1950-2014 mean.

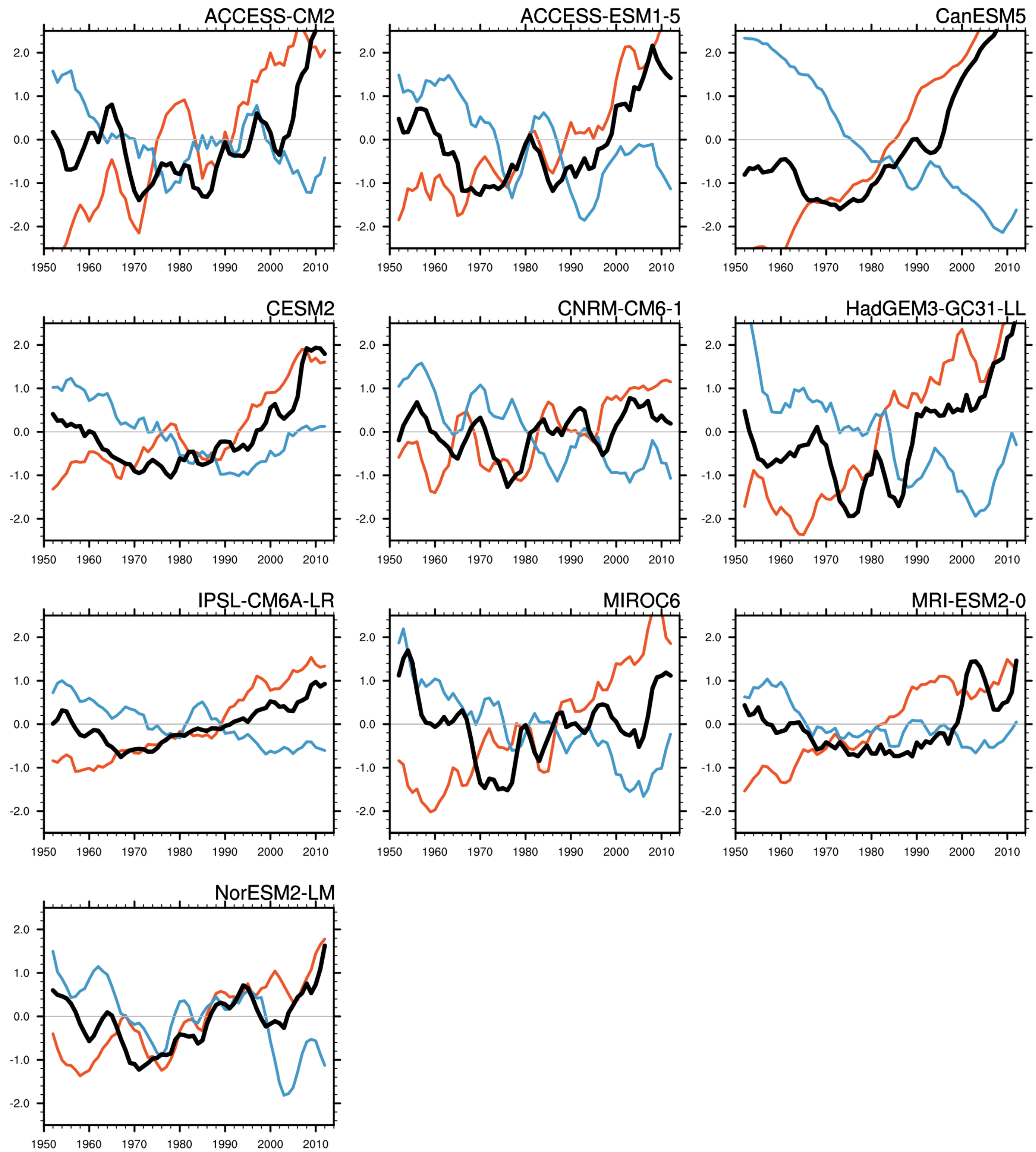

Fig. S10. As in Fig. S9, but for the time series of the winter outcrop latitudes (dLat).

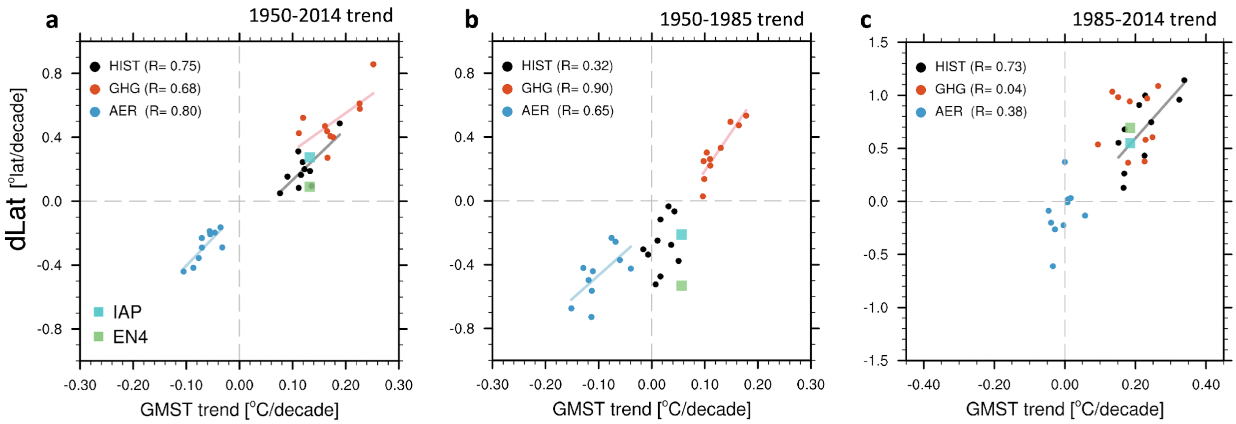

Fig. S11. Scatterplot for dLat against the global mean surface temperature (GMST) trend during (**a**) 1950-2014, (**b**) 1950-1985, and (**c**) 1985-2014. Each dot represents the result from each model ensemble mean. Squares are results from observations. ERA5 2 m air temperature data were used to calculate the observed GMST trend. The correlation coefficients across models are shown in the bracket. The regression line is drawn when the regression is significant at the 95% confidence level.

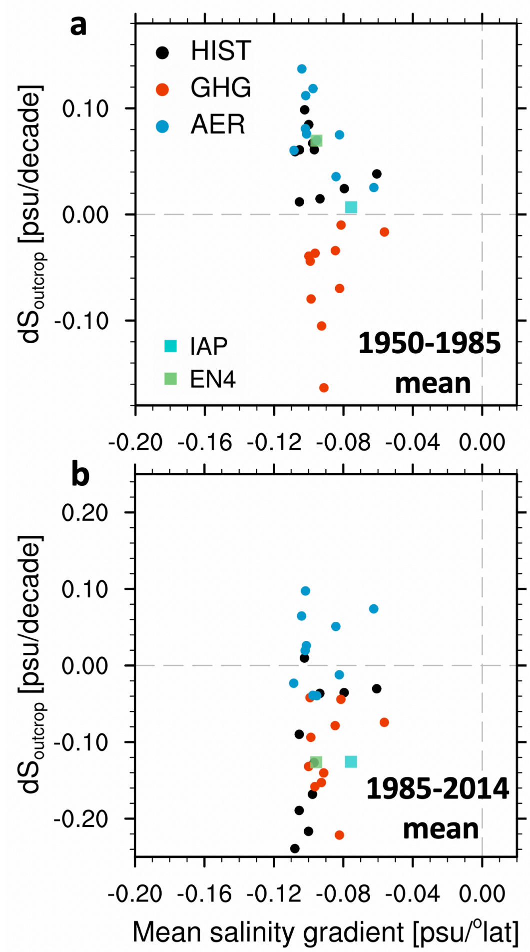

Fig. S12. Scatterplot for $dS_{outcrop}$ against the mean salinity gradient at the surface salinity front in the North Pacific. (**a**) and (**b**) show the mean salinity gradient and $dS_{outcrop}$ during 1950-1985 and 1985-2014, respectively. Each circle represents the result from each model ensemble mean. Squares are estimates from the observation products.